ELSEVIER

#### Contents lists available at ScienceDirect

## Ultrasonics

journal homepage: www.elsevier.com/locate/ultras



## An economic photoacoustic imaging platform using automatic laser synchronization and inverse beamforming



Yixuan Wu<sup>a</sup>, Haichong K. Zhang<sup>a</sup>, Jeeun Kang<sup>a,b,\*</sup>, Emad M. Boctor<sup>a,b,c,\*</sup>

- <sup>a</sup> Department of Computer Science, The Johns Hopkins University, Baltimore, MD 21218, USA
- b Russell H, Morgan Department of Radiology and Radiological Science, The Johns Hopkins University, Baltimore, MD 21218, USA
- <sup>c</sup> Department of Electrical and Computer Engineering, The Johns Hopkins University, Baltimore, MD 21218, USA

#### ARTICLE INFO

Keywords: Photoacoustic imaging Asynchronous Inverse beamforming

#### ABSTRACT

We present a proof-of-concept of an automatic integration of photoacoustic (PA) imaging on clinical ultrasound (US) imaging platforms. Here we tackle two critical challenges: the laser synchronization and the inaccessibility to the beamformer core embedded in commercial US imaging platform. In particular, the line trigger frequency (LTF) estimation and the asynchronous synthetic aperture inverse beamforming (ASAIB) were developed and evaluated in both k-Wave simulation and phantom experiment. The proposed method is an economical solution to enable PA imaging on a greater number of US equipment to further thrive the PA imaging research community.

#### 1. Introduction

Biomedical photoacoustic (PA) imaging is non-invasive and versatile. Its rich optical contrast in functional and molecular features of deep biological tissues secures its remarkable potential in diagnostics, therapeutic monitoring, and surgical guidance [1,2]. With the rapid development in the field, various imaging configurations emerged from scientific investigation to clinical diagnosis, i.e., PA microscopy (PAM) [3,4], intravascular PA imaging (IVPA), endoscopic PA imaging (EPA), PA tomography (PAT) [5,6], and cross-sectional PA imaging [7,8]. The image contrast of PA imaging is either from endogenous absorbers such as hemoglobin, melanin, and early cancer indicators, or from exogenous contrast agents such as molecular dyes [9,10], nanoparticles [11–13], modified microbubbles, and genetically encoded reporters [14], etc. In addition, a novel PA application is being expanded as a guidance tool in interventional radiology, providing higher registration accuracies at sub-mm resolution levels thanks to its acoustic imaging depth and speckle-free contrast resolution [15-18].

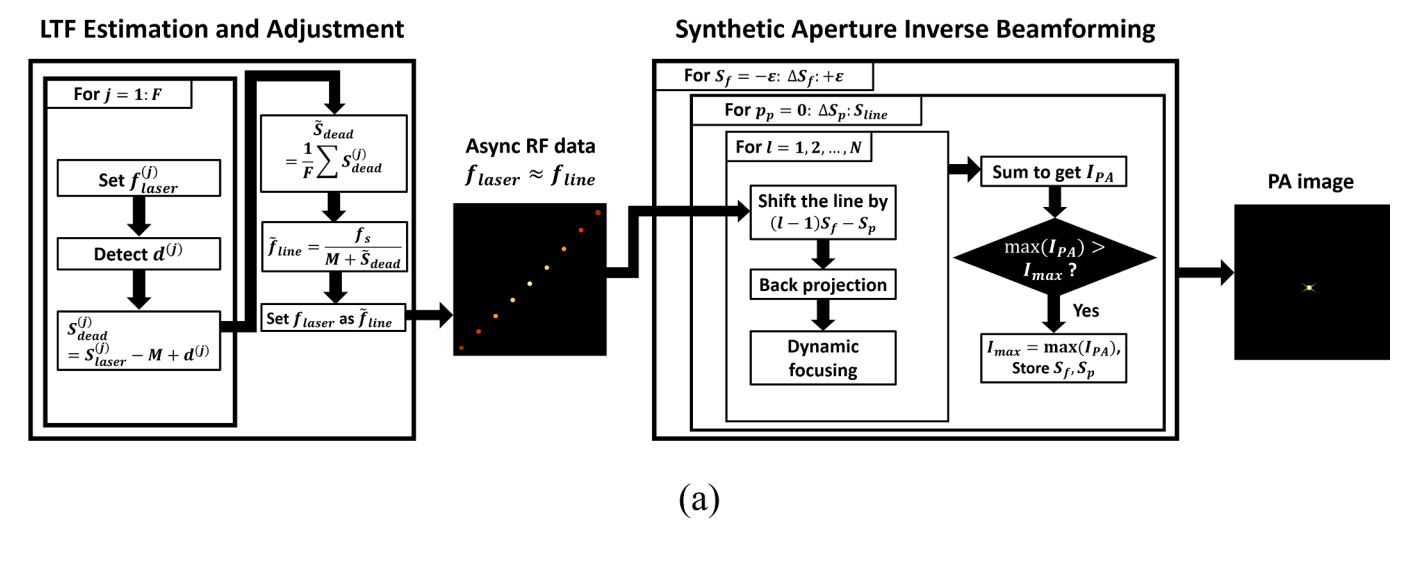
There have been several commercialized PA imaging systems for scientific research communities, e.g., Nexus 128 and 128 + (ENDRA Life Sciences Inc, USA) [19,20], LOIS 3D [21] and LOUISA-3D [22] (TomoWave Laboratories Inc., TX, USA), and Vevo LAZR-X [23] (FUJIFILM VisualSonics Inc., Ontario, Canada). Besides, a high-sensitive cross-sectional PA imaging configuration has been leading the research progress for clinical translation, because general array

transducers (e.g., 2–10 MHz) for clinical ultrasound (US) scanners provide a substantial overlap on the bandwidth of the PA waves [24,25]. From this motivation, several commercial PA imaging systems have presented: MSOT Acuity (iThera Medical GmbH, München, Germany) [21] and Imagio® Breast Imaging System (Seno Medical Instruments Inc., TX, United States) [26,27]. In all the PA imaging systems aforementioned, having accessibility to raw channel data and hardware-synchronization to a pulsed laser source have been regarded as premise features in US imaging platforms.

The most common architecture for the cross-sectional PA imaging is to append commercial US research platforms adjustable for dual-modal US/PA imaging. On one hand, most of the existed products are research-oriented or preclinical platforms built on top of US open platforms that provide transmission-off mode, accessible pre-beamformed channel data, and real-time imaging. Kang, et al. presented real-time tri-modal imaging system, integrating PA, US, and fluorescence imaging, for real-time SLN biopsy guidance at 20 fps using ultrasound DAQ research platform (SonixTouch and SonixDAQ, Ultrasonics Corp., Canada) [29,30]. Cheng, et al. [19,31] acquired PA images at 0.33 fps of landmarks on soft tissue for US-video registration on the Sonix DAQ platform together with MUSiiC toolkit. The Vantage US research platform [32] (Verasonics Inc, USA) also provides a flexible solution of hardware-synchronization and revisable beamforming capability. Wei, et al. studied real-time PA guidance of needle insertion at 30 fps using 720-Hz laser diode-pumped Q-switched laser source [33]. Kim, et al.

E-mail addresses: kangj@jhmi.edu (J. Kang), eboctor1@jhmi.edu (E.M. Boctor).

<sup>\*</sup> Corresponding authors.



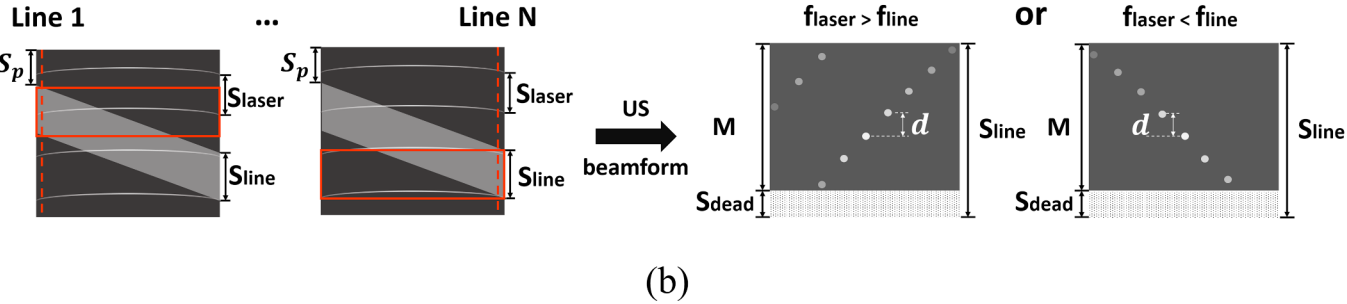


Fig. 1. (a) The overall procedure of software synchronization and asynchronous inverse-beamforming on US-beamformed data. (b) Asynchronous image formation process. Specifically, when  $f_{laser} > f_{line}$ , the wavefront inclines upwards and when  $f_{laser} < f_{line}$ , the wavefront declines downwards.

and Sivasubramanian, et al., presented research platform for dualmodal US/PA imaging using a FleXcan platform (Alpinion Medical Systems Co., Ltd., Seoul, South Korea) [34,35]. More details about the development and the state-of-the-art of US open platforms can be found in E Boni et al. [28]. These approaches provide simple and hassle-free solutions. However, they elevate the entry for many researchers due to high cost of these commercial solutions. On the other hand, there have been several researches that tried to modify clinical US scanners for PA imaging applications. Kim et al. [36] and Erpelding et al. [37] combined PA imaging and US imaging on a modified clinical US scanner (iU22, Philips Healthcare, Netherlands), in their research to detect sentinel lymph nodes (SLN) in vivo. Yang, et al. exploited another clinical US system (Resona 7 [38], Mindray Medical International Limited, China) for thyroid cancer detection [39]. However, the approach also necessitated extensive hardware/software modification for real-time raw channel data acquisition and hardware-synchronization to external triggering, which requires special collaboration with a manufacturer at extensive cost and time. Otherwise, the revision ended up incomplete and image reconstruction had to be performed offline. In particular, providing the RF channel data in real-time would be indeed a big burden for hardware-based US scanners retired from hospitals after tens of years of use, especially when considering their limited data transfer speed available to external devices - Usually a clinical US scanner does not spare or equip with any high-speed data transfer protocol for external workstations (e.g., PCI express). Contrarily, the modification could be minimized in software-based US scanners, but the platform just debuted in the US diagnostic field, so that manufacturers are conservative to open or modify the platform for PA imaging research non-profitably.

In all, the prosperity of the PA research community has been hampered by an economical burden on researchers, whereas broad

investigations are still desired for its successful translation into clinics. We claim here that the ideal solution would be using clinical hardware-based US scanners refurbished or retired from hospitals, while avoiding any extensive system revision to have full accessibility to raw channel data and hardware synchronization to a laser system. Now, this approach clearly arises two critical challenges: (1) Most clinical US scanners provide neither the hardware nor the software triggering solutions, which is required for proper PA data acquisition and receive-beamforming. (2) An irreplaceable built-in US beamformer performs two-way focusing, compensating both acoustic transmitting and receiving propagation time, while a PA beamformer only needs one-way focusing in receiving pathway.

In this proof-of-concept study, we tackle the above two challenges via an economic PA imaging platform solution towards broader research communities. Our method will need neither peripheral hardware for laser synchronization nor the significant modification of a clinical US scanner. Instead, software synchronization will be achieved by estimating asynchrony from US-beamformed radiofrequency (RF) data, and an asynchronous synthetic aperture inverse beamforming (ASAIB) will be applied to reconstruct PA images from the US-beamformed PA signal [40–43].

#### 2. Methods

#### 2.1. Overview

In the following, all variables are in the unit of sample for convenience of calculation. Variables in the frequency domain, the sample domain, and the image domain are denoted by f, S, and I, respectively, where the sample domain is a linear projection of the temporal domain by a factor of  $1/f_s$ ,  $f_s$  is the sampling frequency. All images contain M

rows laterally (x) and N columns axially (z) unless specified. The subjects are differentiated by subscripts, for instance, the pulse repetition frequency (PRF) and the line trigger frequency (LTF) are denoted by  $f_{laser}$  and  $f_{line}$ , respectively. We assume the transducer is centered at the origin position (x = 0; z = 0). Fig. 1a presents the overall workflow of the proposed method. Generally, software synchronization solves for two unknowns: the frequency difference and the phase delay between the line trigger and the pulse repetition (denoted as  $S_f$  and  $S_n$ ), and is performed in two stages: (1) Estimate  $f_{line}$  by equivalently estimating the deadtime  $S_{dead}$ , where  $S_{dead} = S_{line} - M$ . In this stage, we tune the pulse repetition into several different frequencies. For each  $f_{laser}^{(j)}$  $(j = 1, \dots F)$ , we estimate a  $S_{dead}^{(j)}$  using the distance  $d^{(j)}$  between two signal peaks in the adjacent lines. By averaging all  $S_{dead}^{(j)}$ 's, we obtain the estimated  $\tilde{S}_{dead}$  and thereby  $\tilde{f}_{line}$ . (2) Solve for  $S_p$  and the residual frequency error. The two unknowns are grid-searched in ASAIB, until the amplitude of the reconstructed PA image  $(I_{PA})$  is maximized.

Fig. 1b further explains the parameters in PA image data when considering asynchronous data acquisition. If there is a phase delay between the laser excitation and the data acquisition, the laser pulse either leads or lags the receive sampling. Suppose the initial phase delay is  $S_p$  ([sample], positive value means the line trigger leads) and the frequency difference is  $S_f = S_{laser} - S_{line}$  ([sample], positive value means the line trigger has a higher rate). If the start of the receiving in the first line is regarded as time 0, then in line l ( $l = 1, \dots, N$ ), the lag between the pulse repetition and the line trigger is

$$S_{lag}(l) = S_p + (l-1)S_f$$
 (1)

No matter if  $S_{lag}$  is positive or negative, the beamformer is blind and will produce significant beamforming error.

In summary, we need to know  $S_{laser}$  and  $S_{line}$  to estimate  $S_f$  and  $S_p$  for automatic software synchronization between the laser and the US imaging system. We assume here that  $S_{laser}$  is known since it is provided by the laser system, and an energy meter needed for securing biosafety can usually provide the instantaneous PRF measurement. Thus, the problem is determined by two unknowns, i.e.,  $S_{line}$  and  $S_p$ .

#### 2.2. Asynchronous ultrasound-beamformed photoacoustic imaging

This section introduces basic principles of the conventional and proposed PA imaging system operations, based on simplified illustrations using a five-element linear array probe model for a single point target (Fig. 2). A comparison will be provided between (1) synchronous PA imaging on a US research platform, (2) synchronous PA imaging on a US scanner with irreplaceable US beamformer, and (3) asynchronous PA imaging on a clinical US scanner with irreplaceable US beamformer and the absence of hardware synchronization. In each scenario, simple delay-and-sum (DAS) beamforming with dynamic focusing is assumed.

Let us first focus on how PA signals are imaged by a fully customized US research platform (Fig. 2a). In 2a(i), periodic laser pulses are indicated by arrows along the temporal axis. Upon a laser pulse is emitted, the hardware synchronization between the laser and the US platform triggers the data acquisition (i.e.,  $f_{laser}$  equals  $f_{line}$  and there is no phase delay), as shown in 2a(ii). The focusing delay for dynamic receive beamforming will be applied to each channel as indicated in 2a (iii) and 2a(iv), producing the delayed channel data as presented in 2a (v). Finally, by concatenating all A-lines, the post-beamformed RF data is attained in 2a(vii).

Fig. 2b demonstrates the second scenario, which is synchronous PA imaging on a US scanner with irreplaceable US beamformer. Fig. 2a and Fig. 2b start to differ from (iv), that the embedded beamformer would compensate the time-of-flight (TOF) in a two-way trip for US imaging, rather than receive-only required by PA imaging. Due to the incorrect delay function, each channel data is over-delayed with an amount of transmit TOF, producing a semi-focused curve in the post-beamformed data when summed among channels.

Fig. 2c demonstrates a practical scenario of an asynchronous PA imaging on a clinical US scanner without any flexibility in both laser synchronization and beamforming. It yields two main components of misalignments: one is the frequency difference ( $|f_{laser} - f_{line}|$ ), and the other is the phase delay. For example, Fig. 2c illustrates the situation when  $f_{laser} > f_{line}$ . In this case, a single line starts to include multiple PA wavefronts generated by multiple laser pulse excitations as shown in 2c (ii) and (iii). The post-beamformed RF data becomes not only semi-focused, but also discrete, spreading as broken spots instead of a continuous wavefront.

More formally, we give a mathematical description of the three scenarios. To make clear the difference between PA beamforming and US beamforming, we consider all the imaging processes in the sample domain. Denote the pre-beamformed RF channel data as  $I_c \in \mathbb{R}^{M \times N}$ , the US-beamformed RF data as  $I_{US} \in \mathbb{R}^{M \times N}$ , and the PA-beamformed RF data as  $I_{PA} \in \mathbb{R}^{M \times N}$ . Suppose the sample spacing and the element spacing (i.e., pitch) are  $\xi_z$  and  $\xi_x$  ([m]), respectively. For the PA beamformer, the delay  $\tau_{PA}$  ([sample]) in line index l ( $l=1, \cdots, N$ ) and focus depth index j ( $j=1, \cdots, M$ ) for channel index i ( $i=1, \cdots, N$ ) can be equated by

$$\tau_{PA}(l,i,j) = \frac{1}{\xi_z} (\sqrt{((i-l)\cdot\xi_x)^2 + (j\cdot\xi_z)^2} - j\cdot\xi_z) = \sqrt{((i-l)\cdot\xi_x/\xi_z)^2 + j^2} - j$$
(2)

And the PA image at (l, j) is formulated by

$$I_{PA}(l,j) = \sum_{i=1}^{N} w(\tau_{PA}, l, j) \cdot I_{C}(\tau_{PA}, l, j)$$
(3)

where  $w(\tau_{PA}, l, j)$  is the apodization weight.

Considering US beamforming on the PA data, each dynamic focus is at half of the physical depth of PA beamformer's due to additional transmit time-of-flight compensation. Therefore,

$$\tau_{US}(l, i, j) = \sqrt{((i - l) \cdot \xi_x / \xi_z)^2 + (j/2)^2} - j/2$$
(4)

$$I_{US}(l,j) = \sum_{i=1}^{N} w(\tau_{US}, l, j) \cdot I_{C}(\tau_{US}, l, j)$$
(5)

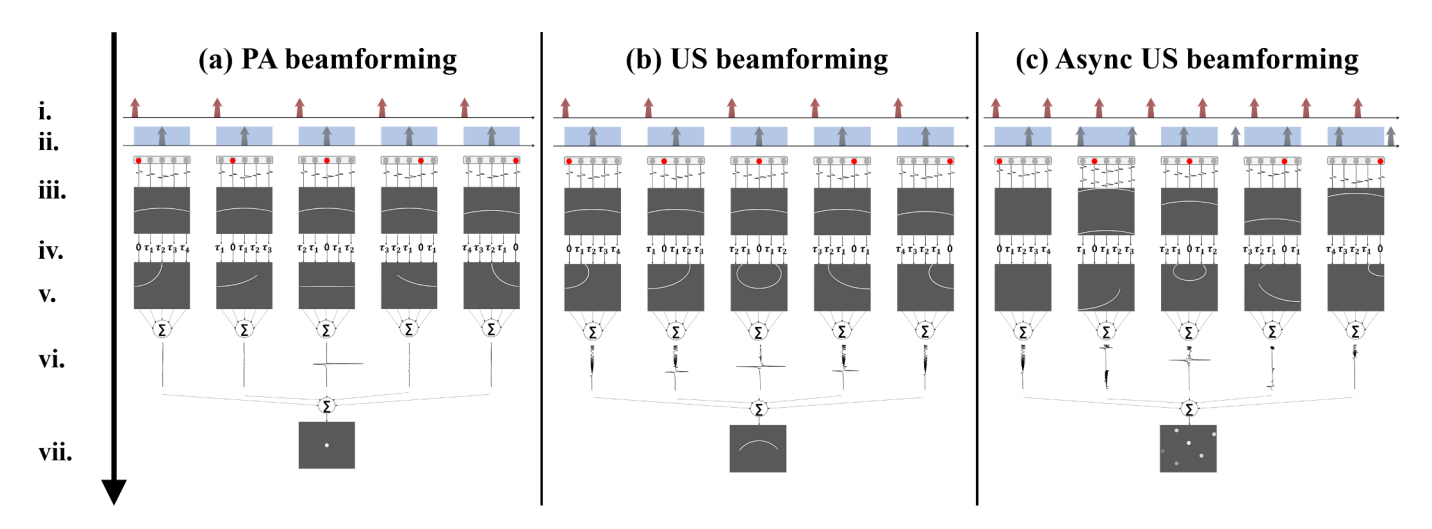
#### 2.3. Line trigger frequency estimation

Intuitively,  $S_{line}$  should be directly reflected by the axial dimension M. However, on clinical US machines, a deadtime  $S_{dead}$  is internally determined, making  $S_{line} = M + S_{dead}$ . We propose to estimate  $S_{dead}$  using the asynchronous US beamformed images of a point target. Even though the US beamformed PA data is highly deformed as discrete peaks, the axial distance between the two consecutive peaks in the adjacent lines provides useful information about  $S_f$ . Denote the distance between the subsequent peaks of PA intensities in line l and (l+1) as d(l) we have

$$S_f = S_{laser} - S_{line} = d(l) + o(l)$$
(6)

where o(l) is a deformation term introduced by the incorrect beamforming on the single point-target and the timing jitter of the laser source (e.g. Cole et al. reduced the standard deviation of the pulse-pulse timing jitter on a passive Q-switched Nd:YAG laser from 241 ns to 20 ns [44]). In software synchronization, the laser timing jittering error is inevitable. However, any jitter less than one half of the transducer sampling resolution (e.g., for 40 MHz sampling rate the sampling resolution is 25 ns) is negligible. Moreover, since the jitter is generally zero-mean [43], imaging is stable over time. On the other hand, in order to minimize the deformation factor o(l), we select the line  $l_{max}$  which is the lateral position of the image amplitude, since it implies the lateral position of the single point-target. Therefore,  $S_{dead}$  is obtained by substituting  $S_{line}$  in Eq. (6) with  $(M+S_{dead})$ , which is given by

$$S_{dead} = S_{laser} - M - d(l_{max}) \tag{7}$$



- i. Laser pulse repetition ii. Receive sampling iii. Channel data
- ii. iv. Adding delay v. Delayed data vi. A-lines vii. Beamformed RF data

Fig. 2. PA image formation process of a single point-target source. (a) PA imaging on a custom US research platform, (b) synchronous PA imaging on a US scanner with irreplaceable US beamformer, and (c) asynchronous PA imaging on a clinical US scanner. (a), (b), and (c) all follow the steps from (i) to (vii). (i) and (ii) indicate the timing diagram of laser pulse excitation and signal reception. The red elements in (ii) are the center of the receive aperture with 5 elements. (iii) to (vii) are channel data, focusing delay function, delayed data, beamformed A-lines, and post-beamformed data, respectively. (iii) and (iv) are the channel data collected over time; (vi) and (vii) are shown in A- and B-mode, respectively. (For interpretation of the references to colour in this figure legend, the reader is referred to the web version of this article.)

To avoid the strongest peak falls into the deadtime zone, we measure multiple  $\delta$ 's in multiple frames and average them to estimate  $\widetilde{S}_{dead}$ . Thereafter it is easy to obtain  $\widetilde{f}_{line} = f_s/\widetilde{S}_{line} = f_s/(M + \widetilde{S}_{dead})$ .

# 2.4. Optimization with asynchronous synthetic aperture inverse beamforming

This section introduces an optimization problem which solves for both  $S_p$  and the residual frequency error  $(S_f - \widetilde{S}_f)$  using ASAIB method based on a synthetic-aperture-based re-beamforming (SPARE [22,23]). The workflow of ASAIB is shown in Fig. 3. The difference of ASAIB from SPARE is the asynchrony. To find out the relation between US-

beamformed PA signal and the true PA images, let us consider the receive fixed focusing scenario. In fixed focusing, only focal depth produces most coherent beamforming performance. Now consider the US beamformer, where each summation of the transmit and the receive focusing delay would be approximately doubled compared with that of PA beamformer at certain focusing depth. Thus, the US-beamformed PA data are as if they were transmitted from the fixed focusing point at half of the dynamic focus depth. In SPARE, for any dynamic focal point at depth  $z_f$  ([sample]), it satisfies

$$z_f = j/2 (8)$$

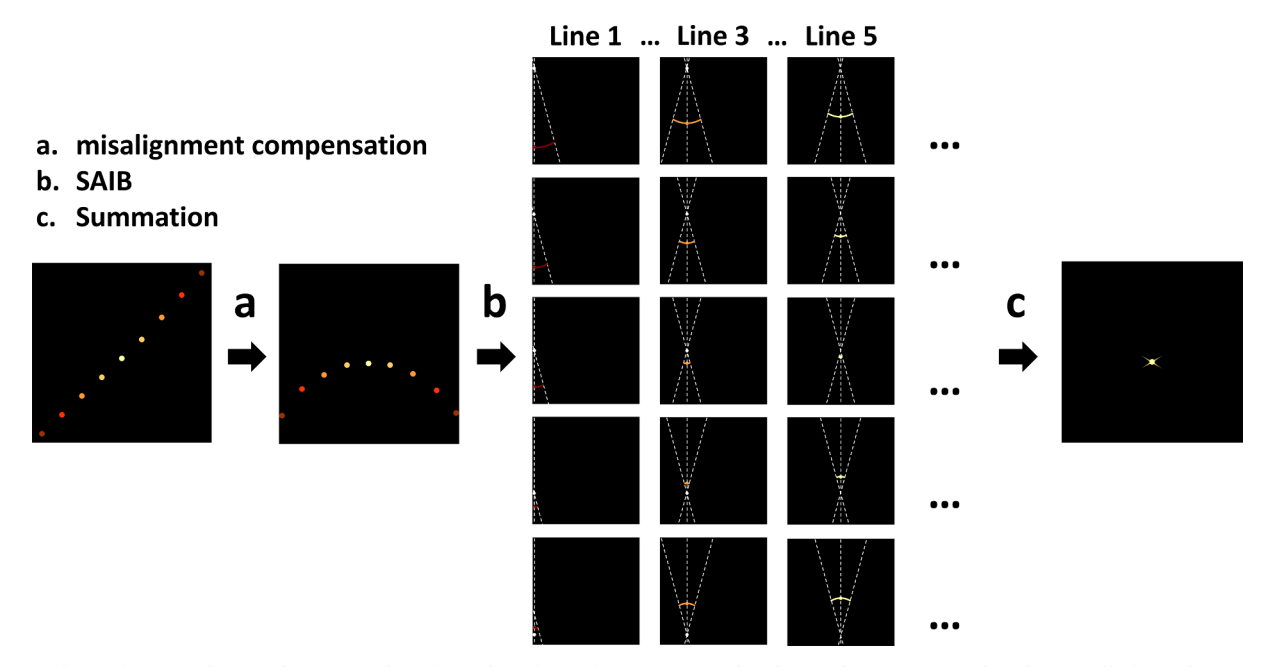


Fig. 3. Procedures of ASAIB. The asynchronous US-beamformed RF data is first compensated with  $S_f$  and  $S_p$  in step (a), then dynamically focused in step (b). The white dotted lines crossing at the focus outlines the beam profile. (c) is the summation of all the delayed signal to get the reconstructed PA image.

$$\tau_{SPARE}(l, i, j) = \sqrt{((i - l) \cdot \xi_x / \xi_z)^2 + (j - z_f)^2} - z_f$$
(9)

To take account of the asynchrony, ASAIB first realigns the asynchronous RF data  $I_{RF}$  such that,

$$\bar{I}_{RF}(l,j) = I_{RF}(l,j+(l-1)\cdot(S_f - \tilde{S}_f) - S_p)$$
(10)

where  $\bar{I}_{RF}(l,j)$  is the aligned data, and zeros are padded at the beginning or the end of the shifted lines to keep the image dimension. The focus depth with respect to the coordinates of  $\bar{I}_{RF}$  is given by

$$\bar{z}_f = j/2 - ((l-1)\cdot(S_f - \tilde{S}_f) - S_p)$$
(11)

And the delay function and the reconstructed PA image are equated by

$$\tau_{ASAIB}(l, i, j) = \sqrt{((i - l) \cdot \xi_x / \xi_z)^2 + (j - \bar{z}_f)^2} - \bar{z}_f$$
 (12)

$$I_{ASAIB}(l,j) = \sum_{i=1}^{N} w(\tau_{ASAIB}, l, j) \cdot \bar{I}_{RF}(\tau_{ASAIB}, l, j)$$

$$\tag{13}$$

Note that  $S_p$  and  $S_f$  are unknown, we estimate them by solving an optimization problem,

where  $\varepsilon$  is a tolerance parameter of residual frequency error  $(S_f - \overline{S}_f)$  produced during the LTF estimation. The US-beamformed RF data have highly oscillating intensity over PA signal duration in axial direction, and the term o(l) in Eq. (6) will possibly introduce a small error when automatically searching for the  $\delta(l_{max})$  in Eq. (7). The heuristic optimization in Eq. (14) will eliminate the residual frequency error.  $\mathscr F$  is a metric function such as the maximum value or the sharpness [45]. Since the optimization problem is highly non-convex, we grid-search to solve for  $S_f$  and  $S_p$  and define  $\mathscr F$  as  $\max(I_{ASAIB})$  to reduce time complexity.

Note that our method does not confine the PA image beamforming method in subsequent applications to DAS. The purpose of the proposed ASAIB algorithm is to synchronize the laser system and the US platform beforehand. Once the laser and the US platform are synchronized, any beamforming algorithm can be used for PA image formation.

#### 3. Results

## 3.1. Simulation

## 3.1.1. Generation of channel data

Pre-beamformed RF channel data of a single point target was generated using k-Wave toolbox in MATLAB (Mathworks, Inc., MA, United States), and the US-beamformed frame was reconstructed (Fig. 4a and b) [46]. A 1-D linear array probe with 128-elements and 0.385-mm element pitch samples uniformly in the frequency domain and works in the receive-only mode. The imaging field-of-view was designed to be 60-mm wide by 50-mm deep, surrounded by a 2/3 λ-thick perfectly matched layer (PML), where the transducer is assumed to be at 0 depth and centered in the imaging field-of-view in lateral direction. All computation was done in a spatial grid in step of  $1/6 \lambda$ , and a time grid in step of 25 ns (40 MHz sampling frequency). Homogenous tissue fills up the imaging domain, where the medium speed of sound was at 1540 m/s with 1020 kg/m<sup>3</sup> of the medium density. A point target in radius of  $1/8 \lambda$  with the medium density doubled from the surrounding tissue was positioned at (0, 25) (mm). An initial pressure was set on the target, and the temporal signal in channel 64 and its frequency spectrum is shown in Fig. 4(a). We assumed that the imaging depth in US imaging system is set identical to the target imaging depth in PA imaging, which will collect the data amount about two-times from that required for the PA imaging depth. The above parameters yield  $M = zf_s/c = 1$ , 299 (sample) and  $f_{line} = c/2z = 15.4$  (kHz), where z is the

imaging depth. Thus,  $S_{dead}$  is 1300 samples given by  $f_s/f_{line} - M$ .

#### 3.1.2. Generation of asynchronous US-beamformed RF data

In simulation, the true LTF is set as 15.4 kHz and the phase delay is set as + 0.1 $\pi$  radians. PRF was tuned into different values to estimate  $S_{dead}$ . One asynchronous US-beamformed data is illustrated in Fig. 4b, where  $f_{laser}=1.27$  kHz and  $f_{line}=19.56$  kHz.

#### 3.1.3. The line trigger frequency estimation

To estimate LTF, PRF is tuned into 9 different values from 12.0 kHz to 20.0 kHz in 1.0 kHz step, where 9 frames of asynchronous US-beamformed RF data were obtained under each PRF. Note that our LTF estimation algorithm was blind to these predefined LTF values to mimic the realistic circumstance with unknown PRF. In frame  $(j=1,\cdots,9)$ ,  $S_{dead}^{(j)}$  is estimated by estimating  $d_j$  using z-score peak detection algorithm [24], as shown in Table 1. By averaging 9 estimations of  $S_{dead}$  values,  $\widetilde{S}_{dead}$  is estimated to be 1298 samples. This led to  $\widetilde{S}_{line}$  equal to 2597 samples, corresponding to  $\widetilde{f}_{line}$  at 15.401 kHz. Thus, the PRF is adjusted as  $f_{laser} = \widetilde{f}_{line} = 15.401$  kHz. The asynchronous US-beamformed data using the estimated LTF is shown in Fig. 4c. On a 4-core i7 8th Gen CPU laptop, the simulation of the asynchronous US-beamformed images and the LTF estimation under nine frequencies takes 62 s in total on average.

To evaluate the robustness of the algorithm to the laser timing jitter, we tested five different levels of jitters, where the distribution of the jitter is assumed to be random Gaussian, with 0 mean and standard deviation of 0, 25 ns, 100 ns, 250 ns, 500 ns, respectively. Fig. 4(l) shows the simulation result of 100 runs, where the average and the standard deviation of the deadtime estimation for 0, 25 ns, 100 ns, 250 ns, and 500 ns are 1300  $\pm$  0.39, 1,303  $\pm$  0.50, 1,302  $\pm$  0.94, 1,302  $\pm$  1.42, 1,301  $\pm$  1.67, respectively. Therefore, the algorithm shows good accuracy and robustness to different levels of laser timing jitter.

#### 3.1.4. Asynchronous synthetic aperture inverse beamforming

In the ASAIB, two important variables,  $S_f$  and  $S_p$ , are linearly optimized by grid search.  $S_f$  is optimized in steps of 1 sample within a range of  $\pm 10$  samples, and  $S_p$  is optimized in steps of 5 samples, in a range of the whole duty cycle of  $\pm$  0.5 $M = \pm 650$  samples.  $S_f$  and  $S_p$  were solved as + 2 samples and + 130 samples, respectively. Therefore, the LTF was estimated as  $f_s/(\tilde{S}_{line} + S_f) = 15$ . 40 kHz, and the phase delay was estimated as  $(S_p/\tilde{S}_{line} + S_f)\cdot 2\pi = 0$ . 100039 $\pi$ , where the estimation error was 0 and 0.039% for frequency and phase, respectively. By compensating the image in Fig. 4c with the calculated misalignment, an aligned image is shown in Fig. 4d. Finally, by beamforming the image in Fig. 4d synthetically using uniform apodization, we retrieved the PA image of the single point-target source in Fig. 4f. Compared with the ground truth with PA beamforming (Fig. 4e), Fig. 4f has large side lobes. By using Blackman apodization in ASAIB, side lobes were much suppressed as demonstrated in Fig. 4g. Fig. 4i, j, and k are contour plots of the region of interest (ROI) from (19.00, 19.00) (mm) to (31.00, 31.00) (mm) in Fig. 4e, f, and g, respectively. They better show the image resolution and the side lobes. The amplitudes of Fig. 4e, f, g were detected at (25.03, 24.99), (25.03, 24.87), and (25.03, 24.87) (mm), respectively, where the PA source was mispositioned by (0, 0.46%) in both 5f and 5 g. As indicated in Fig. 4h the full width half maximum (FWHM) is measured as 0.93, 1.11, 1.55 (mm) for the ground truth, ASAIB with uniform apodization and ASAIB with Blackman apodization, respectively. In simulation, each iteration of the grid search takes 0.20 and 3.85 s in average on a 4-core i7 8th Gen CPU laptop for the uniform apodization and Blackman apodization, which leads to a total running time of 17 min and 5.5 h, respectively.

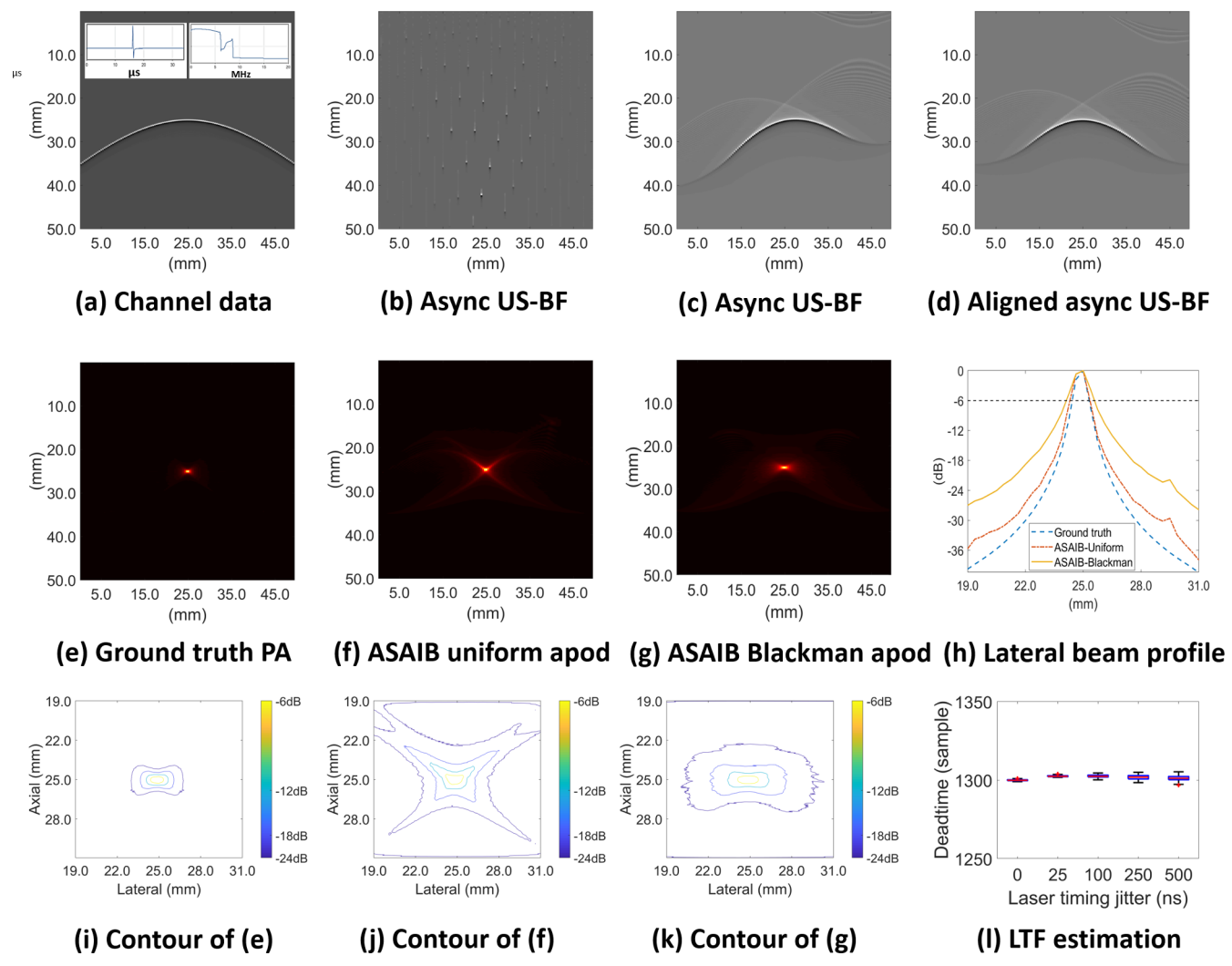


**Fig. 4.** Simulation results. (a) Channel data. The temporal signal in channel 64 and its frequency spectrum is shown upper left and right, respectively. (b) Asynchronous US-beamformed RF data, where  $f_{laser} = 1.27f_{line}$  and the phase delay is  $0.3\pi$  radians (line trigger leads). (c) The resulted US beamformed RF data after LTF estimation, where  $f_{line} = 15.401$  kHz and the true LTF is  $f_{line} = 15.400$  kHz. (d) The resulted image where the misalignment is compensated line by line from (c). (e) Ground truth PA image, Blackman apodization was considered. (f) Retrieved PA image with uniform apodization. (g) Retrieved PA image with Blackman apodization. (h) The lateral beam profile of the ground truth signal, ASAIB with uniform apodization and ASAIB with Blackman apodization. (i), (j), and (k) are contour plots of the same ROI in (e), (f), and (g), respectively. (l) Box plot of the line trigger frequency estimation result when laser timing jitter exists.

**Table 1**Deadtime estimation result under 9 different PRFs in simulation.

f <sub>laser</sub> (kHz)	12.0	13.0	14.0	15.0	16.0	17.0	18.0	19.0	20.0	Average	Ref
$\tilde{S}_{dead}$ (sample)	1290	1297	1300	1287	1302	1300	1302	1302	1304	$1298.22 \pm 5.89$	1300

#### 3.2. Phantom experiment

### 3.2.1. Ultrasound-beamformed photoacoustic data acquisition

This section investigates the validation via phantom study. The US-beamformed PA data were acquired from an externally triggered Ultrasonix Sonix CEP system. An L12-5 58.5 mm linear array probe worked at receive-only mode, where the sampling rate was 40 MHz and the imaging depth was set at 10 cm. A single PZT element placed in the water tank transmitting 5 MHz central frequency acoustic pulses was used to mimic a single PA point target source. Completely-separated two function generators both yielded 3.5 V, 50% duty cycle square wave to control the  $f_{laser}$  and  $f_{line}$  in the single PZT element and ultrasound systems, respectively. The speed of sound in water was assumed to be 1540 m/s.

#### 3.2.2. The line trigger frequency estimation

We fixed  $f_{line}$  at reasonable value, 3000 Hz, which yields the estimated frame rate at 23.44 Hz when reconstructing 128 lines per frame. This imaging specification gives  $S_{line} = f_s/f_{line} = 13$ , 333. The images obtained from the US machine indicates M=4674, so the true  $S_{dead}=8659$ . To estimate  $f_{line}$ ,  $f_{laser}$  is tuned into 9 different frequencies, under each frequency we obtained 10 different frames of asynchronous US-beamformed data for averaging. Because the  $S_{dead}$  takes a relatively large portion in  $S_{line}$ , when  $f_{laser}$  is too far from  $f_{line}$  a lot of wavefront information is missing in a single frame of image. The averaged deadtime under each frequency is listed in Table 2.

 Table 2

 Deadtime estimation result of a single PZT element phantom study.

$f_{laser}(Hz)$	2700	2800	3000	3140	3200	3300	3400	3700	4130	Average	Ref
$\tilde{S}_{dead}$ (sample)	8,660	8,665	8,659	8,660	8,659	8,661	8,659	8,656	8,648	$8,658.55 \pm 4.61$	8,659

#### 3.2.3. Asynchronous synthetic aperture inverse beamforming

The ASAIB results are shown in Fig. 5. One illustration of the asynchronous US-beamformed image is shown in Fig. 5(a), where  $f_{line}=3140$  Hz. After the line trigger frequency estimation, the laser frequency is tuned and an asynchronous US-beamformed image is shown in Fig. 5(b). Fig. 5(c) and (d) are the ground truth PA image and the reconstructed PA image by using ASAIB with Blackman apodization, respectively. The frequency was optimized as 3000.1 Hz, and the phase delay was optimized to be  $0.055\pi$ . Compared with the ground truth (3000.0 Hz and  $0.067\pi$ ), the estimation error for the line trigger frequency and the initial phase delay are 0.0033% and 17.72%, respectively. The phase estimation has a relatively larger error; however, it can be from the bias of the speed of sound.

Fig. 5(e) shows the FWHM in the lateral direction of the point target, which are 1.92 mm and 2.97 mm for the ground truth and the reconstructed image, respectively. To demonstrate in both directions, the corresponding contour plots for the ground truth and the reconstructed image are demonstrated in Fig. 5(f) and (g).

#### 4. Discussion and Conclusion

In this paper, we presented a proof-of-concept of building an economic PA imaging research system in a clinical US scanner using an automatic software synchronization and ASAIB algorithm. The performance of the proposed method was validated in k-Wave simulation and phantom experiment, both of which demonstrated accurate  $f_{line}$ 

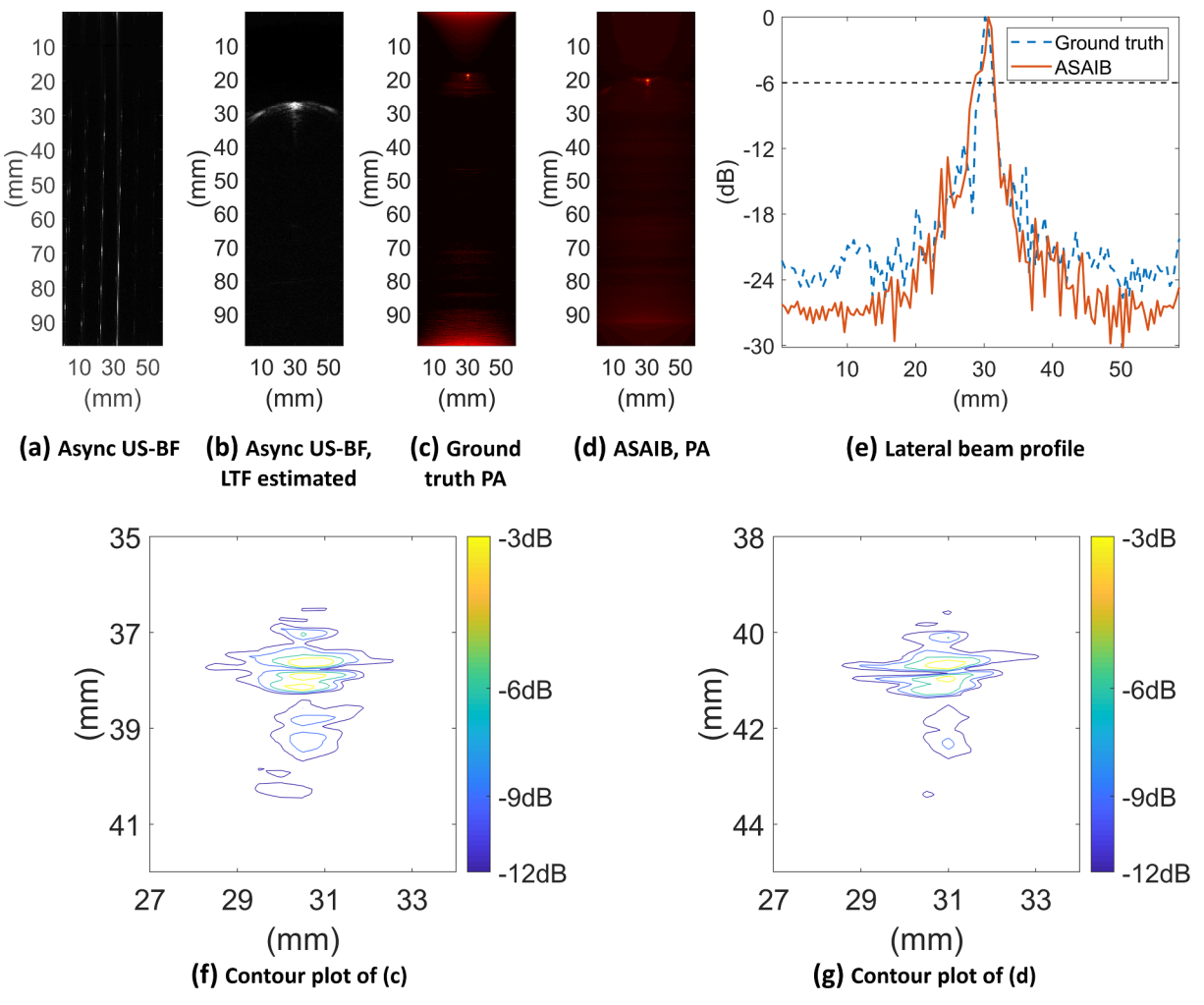


**Fig. 5.** Phantom experiment results. (a) Asynchronous US-beamformed image at  $f_{laser} = 3140$  Hz. (b) Asynchronous US-beamformed image after the line trigger frequency estimation. (c) The ground truth PA image. (d) The reconstructed PA image by using ASAIB. (e) The lateral beam profile of the ground truth PA signal and the ASAIB reconstructed PA signal. (f) Contour plot of the ground truth PA image. (g) Contour plot of the ASAIB reconstructed PA image.

estimation (TABLE 1 and 2). The accurate software synchronization led to comparable spatial resolution to ones in conventional PA imaging using hardware synchronization and dedicated PA beamformer (Figs. 5 and 6).

We envision the prospective protocol with the economic PA imaging platform as follows: (1) Researcher may obtain a refurbished or retired US scanner from hospital or manufacturer with significantly reduced price, and place along with pulsed laser system and workstation. (2) Manufacturer provides the electronic software packet to users, enabling the real-time acquisition of US-beamformed RF data and disenabling US transmittance. (3) Prepare a point-target phantom. Any point-target would provide the capability for software synchronization. (4) Turn on the laser excitation and collect multiple US-beamformed RF data.

Multiple frames exhibiting different PA pressure wavefronts under several ratios of  $f_{laser}$  and  $f_{line}$  are ideal to have accurate  $S_{dead}$  estimation for reliable  $f_{line}$  estimation. (5) Estimate the automatic software synchronization which yields  $f_{line}$ . (6) Apply ASAIB based on the estimated  $f_{line}$  to synchronize the frequency and the phase delay between laser excitation and US data acquisition, and eventually reconstruct the target for PA imaging.

In addition to the scientific research, this method may also have extended applicability to the navigational tools for clinical radiological intervention using spotted PA excitation [17,18]. Having the dedicated US imaging platform fully hardware triggerable and accessible to raw channel RF data would be expensive option for this application. Using the proposed method, one may synchronize the pulsed laser source and retired clinical US scanner, and can track the interventional tool navigating the vasculatures inside patient's body. Moreover, an advanced catheter which can actively communicate with external US imaging transducer can even be supported by the proposed method, instead of pulsed laser source for PA signal generation, without having hardware triggering and accessibility to raw channel RF data [32].

The proposed method is still at the stage of proof-of-concept and there are several limitations to be resolved. First, our current research only presented limited scenarios regarding the rate difference between laser excitation and US data acquisition. We will conduct more comprehensive and realistic cases to secure the reliability of the method, assuming several laser sources at different PRF and its combinational setup with various LTF in an US scanner. Second, though electronic peripherals in between the pulsed laser and the US scanner with accessibility to channel RF data are not needed, the post-beamformed RF data is still required, which is not accessible from all current clinical platforms. Yet we cannot deny that US-beamformed RF data significantly reduces the data throughput for real-time data transfer with the amount of data folded by the number of channels (usually 128–256). For example, consider a 2 bytes/sample, 2048 samples/ channel scenario in a 128-channel US imaging platform, where the data size of a single line is 512 kB and all channels per frame is 64 MB. Thus, channel RF data takes longer to transfer, which reduces the reliability of LTF estimation since the data memory access time is incorporated into the deadtime and PA wavefronts are more likely to fall into the deadtime. Third, this algorithm still runs off-line, which lowers its efficacy in practical investigation of PA imaging for clinical translation. To enable complete real-time investigations on clinical US scanners, the time complexity should be further reduced. This can be achieved by a better optimization method rather than the grid search employed in our method, or by accelerating the computation through parallel programming technique. Moreover, any imaging depth change would

inevitably affect the line triggering. We may consider the scenarios that physicians accidentally change the setting or make an intentional change of imaging depth, then a previously established software synchronization will be no longer effective in the revised imaging depth. Therefore, researchers have to re-synchronize the systems. The automatic detection of these events and recalibration will resolve the problem. Fourth, a problem to be addressed is the jittering effect of the laser system. Current technology has reduced the timing jitter of passive Q-switched Nd:YAG laser from hundreds of nanoseconds to tens of nanoseconds [43], then to picosecond level [47]. Compared with the sampling resolution (tens of nanosecond) of the transducer, this iitter is negligible. Also, thanks to the zero-mean property of the iitter, the synchronized systems will work stably over time. However, we still considered high jittering lasers in the line trigger frequency estimation and developed a robust estimation algorithm. In practice, synchronize the high jittering laser system to the US machines by software in one time is not enough. We consider to include energy-meter real-time monitoring in future work. Finally, our method requires programmable laser system, which is not an option provided by every laser system. We will generalize our method in future work toward fixed-frequency lasers. Possible solution is to tune the imaging depth of the US machine in software to change the unknown line trigger frequency until it converges to the fixed laser frequency, then use ASAIB to recover the phase delay.

In conclusion, we presented an economic PA imaging platform, which will allow broader PA imaging research community to use refurbished or retired US scanner without either hardware synchronization or access to pre-beamformed channel RF data. Compared with the previous approaches using commercial research platforms or extensive collaboration with manufacturers, the range of system modification should be minimized – (1) Real-time access to US-beamformed RF data would be much easier with minimal data throughput requirement when compared to the raw channel data. (2) US transmit-off mode should be just a simple software modification.

## **Declaration of Competing Interest**

The authors declare that they have no known competing financial interests or personal relationships that could have appeared to influence the work reported in this paper.

#### Acknowledgements

This work was supported by National Institute of Heart, Lung and Blood [grant number R01HL139543]; National Institute of Biomedical Imaging and Bioengineering [grant number R01EB021396]; National Cancer Institute [grant numbers R01CA134675 and R44CA192482]; National Institute of Health [grant number DP50D028162]. Yixuan Wu was partially supported by National Institute of Health Graduate Partnerships Program. Jeeun Kang, Ph.D., was partially supported by National Research Foundation of Korea [award number 2018R1A6A3A03011551] and U.S. Department of Defense [award number W81XWH-18-1-0188]. The corresponding author Emad M. Boctor was partially supported by National Science Foundation [award number 1653322]. We also sincerely thank Alexis Cheng for providing ex vivo data for preliminary trials and Younsu Kim for phantom experiment setup.

#### Appendix A

#### **Primary Notations**

Domain	Symbol	Description
Frequency domain (Hz)	$f_s$	Sampling frequency
	$f_{laser}$	Laser pulse repetition frequency
	$f_{line}$	Line trigger frequency
	$ ilde{f}_{line}$	Estimated line trigger frequency
Sample domain (sample)	M M	The number of rows of the image
	N	The number of lines of the image
	$S_f$	The frequency difference between the laser pulse repetition and the line trigger
	$\widetilde{S}_f$	The estimated frequency difference between the laser pulse repetition and the line trigger
	$S_p$	The phase delay between the laser pulse repetition and the line trigger
	$S_{dead}$	The deadtime in each scan line
	$\tilde{S}_{dead}$	The estimated deadtime in each scan line
	$S_{lag}$	The total lag that contributed by the frequency difference and the phase delay between the laser pulse repetition and the line trigger
	d	The distance between two peaks in the adjacent lines
	$\tau_{PA}$	The delay function of PA imaging
	$ au_{US}$	The delay function of US imaging
	$\tau_{SPARE}$	The delay function of SPARE
	$\tau_{ASAIB}$	The delay function of ASAIB
	0	The deformation generated by incorrect beamforming
	ε	The residual line trigger frequency estimation error
	$z_f$	Depth of a receive focus
	Ī.f	Depth of a receive focus after the alignment of the data in ASAIB
Images/data	$I_C$	Channel data
	$I_{PA}$	PA images
	$I_{US}$	US images
	$I_{RF}$	US-beamformed images
	$ar{I}_{RF}$	Aligned US-beamformed images
others	F	Total number of frames used for deadtime estimation
	w	Apodization function
	$l_{max}$	The index of the line containing the image amplitude
	$\xi_x$	Lateral sample spacing (pitch) ([m])
	$\xi_z$	Axial sample spacing ([m])
	F	Metric function for ASAIB optimization

#### References

- Srivalleesha Mallidi, Geoffrey P. Luke, Stanislav Emelianov, Photoacoustic imaging in cancer detection, diagnosis, and treatment guidance, Trends Biotechnol. 29 (5) (2011) 213–221.
- [2] Geoffrey P. Luke, Doug Yeager, Stanislav Y. Emelianov, Biomedical applications of photoacoustic imaging with exogenous contrast agents, Ann. Biomed. Eng. 40 (2) (2012) 422–437.
- [3] Eric M. Strohm, Michael J. Moore, Michael C. Kolios, Single cell photoacoustic microscopy: a review, IEEE J. Sel. Top. Quantum Electron. 22 (3) (2016) 137–151.
- [4] Junjie Yao, et al., High-speed label-free functional photoacoustic microscopy of mouse brain in action, Nat. Methods 12 (5) (2015) 407.
- [5] Jun Xia, Lihong V. Wang, Small-animal whole-body photoacoustic tomography: a review, IEEE Trans. Biomed. Eng. 61 (5) (2014) 1380–1389.
- [6] Lihong V. Wang, Hu. Song, Photoacoustic tomography: in vivo imaging from organelles to organs, Science 335 (6075) (2012) 1458–1462.
- [7] Chulhong Kim, et al., Deeply penetrating in vivo photoacoustic imaging using a clinical ultrasound array system, Biomed. Opt. Express 1 (1) (2010) 278–284.
- [8] Roy GM Kolkman, et al., Real-time in vivo photoacoustic and ultrasound imaging, J. Biomed. Opt. 13 (5) (2008) 050510.
- [9] Vladimir P. Zharov, et al., Photoacoustic flow cytometry: principle and application for real-time detection of circulating single nanoparticles, pathogens, and contrast dyes in vivo, J. Biomed. Opt. 12 (5) (2007) 051503.
- [10] Haichong K. Zhang, et al., Listening to membrane potential: photoacoustic voltagesensitive dye recording, J. Biomed. Opt. 22 (4) (2017) 045006.
- [11] Srivalleesha Mallidi, et al., Multiwavelength photoacoustic imaging and plasmon resonance coupling of gold nanoparticles for selective detection of cancer, Nano Lett. 9 (8) (2009) 2825–2831.
- [12] Moritz F. Kircher, et al., A brain tumor molecular imaging strategy using a new triple-modality MRI-photoacoustic-Raman nanoparticle, Nat. Med. 18 (5) (2012) 820
- [13] Kanyi Pu, et al., Semiconducting polymer nanoparticles as photoacoustic molecular imaging probes in living mice, Nat. Nanotechnol. 9 (3) (2014) 233.
- [14] Joanna Brunker, et al., Photoacoustic imaging using genetically encoded reporters: a review, J. Biomed. Opt. 22 (7) (2017) 070901.
- [15] Zijian Guo, Li Li, Lihong V. Wang, On the speckle-free nature of photoacoustic

- tomography: On the speckle-free nature of photoacoustic tomography, Med. Phys. 36 (9Part1) (2009) 4084–4088, https://doi.org/10.1118/1.3187231.
- [16] Vyas, Saurabh, et al., Intraoperative ultrasound to stereocamera registration using interventional photoacoustic imaging. Medical Imaging 2012: Image-Guided Procedures, Robotic Interventions, and Modeling. Vol. 8316. International Society for Optics and Photonics, 2012.
- [17] Alexis Cheng, et al., Direct three-dimensional ultrasound-to-video registration using photoacoustic markers, J. Biomed. Opt. 18 (6) (2013) 066013.
- [18] Alexis Cheng, et al., Localization of subsurface photoacoustic fiducials for intraoperative guidance, Advanced Biomedical and Clinical Diagnostic and Surgical Guidance Systems XV Vol. 10054 International Society for Optics and Photonics, 2017.
- [19] Nexus 128 + Capabilities, ENDRA Life Sciences Inc, https://endrainc.com/lab/ nexus-128-capabilities.html, date of access: 2018.
- [20] Nexus 128 and 128 + publications, ENDRA Life Sciences Inc, https://endrainc.com/lab/publications.html, date of access: 2018.
- [21] LOIS 3D Pre-clinical Mouse Imaging System, TomoWave Laboratories Inc, http://www.tomowave.com/products/lois-3d-pre-clinical-system/, date of access: 2018.
- [22] LOUISA-3D imaging system for breast cancer research, TomoWave Laboratories Inc, http://www.tomowave.com/products/louisa-3d-clinical-breast-imaging-system/, date of access: 2018.
- [23] Vevo LAZR-X high resolution multi-modal in vivo imaging platform, FUJIFILM VisualSonics Inc, https://www.visualsonics.com/product/imaging-systems/vevolazr-x, date of access: 2018.
- [24] Wonseok Choi, et al., Clinical photoacoustic imaging platforms, Biomed. Eng. Lett. (2018) 1–17.
- [25] Lihong V. Wang, Liang Gao, Photoacoustic microscopy and computed tomography: from bench to bedside, Annu. Rev. Biomed. Eng. 16 (2014) 155–185.
- [26] A breakthrough in breast cancer diagnostic imaging, Seno Medical, https://senomedical.com/, date of access: 2019.
- [27] Wonseok Choi, et al., Clinical photoacoustic imaging platforms, Biomed. Eng. Lett. 8 (2) (2018) 139–155.
- [28] Enrico Boni, et al., Ultrasound open platforms for next-generation imaging technique development, IEEE Trans. Ultrason. Ferroelectr. Freq. Control 65 (7) (2018) 1078–1092.
- [29] Jeeun Kang, et al., Real-time sentinel lymph node biopsy guidance using combined ultrasound, photoacoustic, fluorescence imaging: in vivo proof-of-principle and

- validation with nodal obstruction, Sci. Rep. 7 (2017) 45008.
- [30] Jeeun Kang, et al., A prototype hand-held tri-modal instrument for in vivo ultrasound, photoacoustic, and fluorescence imaging, Rev. Sci. Instrum. 86 (3) (2015) 034901.
- [31] Kang, Hyun Jae. Medical Ultrasound Imaging and Interventional Component (MUSiiC) Framework for Advanced Ultrasound Image-guided Therapy. Diss. Johns Hopkins University, 2015.
- [32] Photoacoustic Research: Advanced Technology for Acquisition and Processing of Ultrasound Signals from the Interaction of Light and Tissue, Verasonics Inc, http:// verasonics.com/photoacoustics/, date of access: 2018.
- [33] Chen-Wei Wei, et al., Real-time integrated photoacoustic and ultrasound (PAUS) imaging system to guide interventional procedures: ex vivo study, IEEE Trans. Ultrason. Ferroelectr. Freq. Control 62 (2) (2015) 319–328.
- [34] Jeesu Kim, et al., Programmable real-time clinical photoacoustic and ultrasound imaging system, Sci. Rep. 6 (2016) 35137.
- [35] Kathyayini Sivasubramanian, et al., Hand-held, clinical dual mode ultrasound-photoacoustic imaging of rat urinary bladder and its applications, J. Biophotonics 11 (5) (2018) e201700317.
- [36] Chulhong Kim, et al., Handheld array-based photoacoustic probe for guiding needle biopsy of sentinel lymph nodes, J. Biomed. Opt. 15 (4) (2010) 046010.
- [37] T.N. Erpelding, et al., Noninvasive photoacoustic and ultrasonic imaging of rat sentinel lymph nodes with a clinical ultrasound system, Radiology 256 (2010)
- [38] The Synergy A new Wave of Ultrasound, Mindray Medical International Limited, http://www.resona7.com/, date of access: 2018.
- [39] Meng Yang, Lingyi Zhao, Xujin He, Na Su, Chen Yang Zhao, Hewen Tang, Tao Hong,

- Wenbo Li, Fang Yang, Lin Lin, Bing Zhang, Rui Zhang, Yuxin Jiang, Changhui Li, Photoacoustic/ultrasound dual imaging of human thyroid cancers: an initial clinical study, Biomed. Opt. Express 8 (7) (2017) 3449, https://doi.org/10.1364/BOE.8. 003449.
- [40] Haichong K. Zhang, et al., Photoacoustic imaging paradigm shift: towards using vendor-independent ultrasound scanners, International Conference on Medical Image Computing and Computer-Assisted Intervention, Springer, Cham, 2016.
- [41] Haichong K. Zhang, et al., Synthetic-aperture based photoacoustic re-beamforming (SPARE) approach using beamformed ultrasound data, Biomed. Opt. Express 7 (8) (2016) 3056–3068.
- [42] Haichong K. Zhang, et al., Software-based approach toward vendor independent real-time photoacoustic imaging using ultrasound beamformed data, Photons Plus Ultrasound: Imaging and Sensing Vol. 10064 (2017).
- [43] Yixuan Wu, Haichong K. Zhang, Emad M. Boctor, Enabling vendor independent photoacoustic imaging systems with asynchronous laser source, Photons Plus Ultrasound: Imaging and Sensing Vol. 10494 (2018).
- [44] Brian Cole, et al., Reduction of timing jitter in a Q-Switched Nd: YAG laser by direct bleaching of a Cr 4+: YAG saturable absorber, Opt. Express 17 (3) (2009)
- [45] Bradley E. Treeby, et al., Automatic sound speed selection in photoacoustic image reconstruction using an autofocus approach, J. Biomed. Opt. 16 (9) (2011) 090501.
- [46] B.E. Treeby, B.T. Cox, k-Wave: MATLAB toolbox for the simulation and reconstruction of photoacoustic wave-fields, J. Biomed. Opt. 15 (2) (2010) 021314.
- [47] Alexander Steinmetz, et al., Reduction of timing jitter in passively Q-switched microchip lasers using self-injection seeding, Opt. Lett. 35 (17) (2010) 2885–2887.